Hindawi
Mathematical Problems in Engineering
Volume 2019, Article ID 9619282, 11 pages
https://doi.org/10.1155/2019/9619282

Research Article

Airflow Patterns around Obstacles with Large-Span Shallow Shell Roof: Wind Tunnel Measurements and Direct Simulation

Hongying Jia, Huixue Dang, Qianying Ma, and Jun-Hai Zhao

School of Civil Engineering, Chang'an University, Xi'an 710061, China

Correspondence should be addressed to Huixue Dang; dhxlxz@126.com

Received 8 June 2019; Revised 7 October 2019; Accepted 18 October 2019; Published 15 November 2019

Guest Editor: Miguel G. Torres

Wind tunnel tests on the rigid model of large-span shallow spherical shell roof structure were carried out. The variation rule and the calculation method for the average shape coefficient of the fluctuating wind pressure under six different typical wind directions were obtained. The wind pressure distribution of the node deflection and cross section stress was numerically investigated and analyzed. Meanwhile, the effect of mechanics-flow form of the typical spherical shell structure on the wind pressure distribution was analyzed quantitatively. In this study, it is found that the results of numerical simulation agree well with the wind tunnel test data. The study on the mechanical characteristics, as well as the wind vibration research, of the spherical shell structure in different working conditions provides a reliable theoretical basis for the mechanical index of the wind vibration.

1. Introduction

Large-span roof structure has been widely used for various large public buildings such as hangars, gymnasiums, and exhibition pavilions in recent decades. The thin shell structure is considered as a great technological progress compared with the large-span roof structure because they can cover a large free area with a roof having a thickness of only a few centimeters [1]. A thin shell is defined as a three-dimensional spatial curved structural surface that is composed of one or more folded plates and curved slabs. Thin shell is recognized as the form-resistant structure that mainly produces bending moment and in-plane stress when subjected to external loads [2, 3]. Due to the aesthetically pleasing surface and reasonable structural form, the shell structure has been widely employed since 1960s. Because of the high strength-to-weight and stiffness-to-weight ratios of these structures and considering the complexity of structural dynamic characteristics, the research on the susceptibility of shell roof subjected to wind loads is of great importance.

Some investigations on the wind-induced dynamic response and stress distribution of large-span roof structures have been performed. Full-scale wind pressure measurement on single-span buildings was conducted by Hoxey and Robertson [4], which indicated that the geometric shape of structure had obvious influences on the wind-induced response of structure. Uematsu et al. [5] studied the wind load characteristics and the mean and fluctuating wind pressures of latticed dome. Fu et al. [6] investigated the effect of wind speed, wind direction, and acceleration responses on the structural performance of roof structures.

Compared with high-rise vertical buildings, the large-span roof structure is featured with its complicated structural frequencies and dynamic resonant responses [7, 8]. Moreover, it is rather complicate to grasp vibration modes of large-span roof structures. Therefore, the extremum of wind-induced responses of large-span shell roof structures cannot be produced only by numerical methodologies. In fact, every single structure has its own special characteristics, and wind tunnel tests of a scaled model are considered essential in order to accurately assess the effect of wind pressure on the large-span structure [9]. Typically, wind tunnel tests are employed to obtain information considering the vibration response or the wind pressure distribution of structures due to the applied wind. Marukawa et al. [10] conducted a series of wind tunnel tests regarding the issue of

fluctuating wind pressures. They discussed the gust loading factor of the large-span roof structures. Hongo [11] investigated the effect of spherical roof's geometry on the characteristics of the wind pressure field in a wind tunnel, and then an empirical formula for assessing the design wind loads was developed. Zhou et al. [12] obtained the experimental tests upon means and fluctuating wind pressures acting on a large roof structure through wind tunnel experiments.

In this study, to determine the mean and fluctuating wind load characteristics, a shallow spherical shell roof structure (with rise-to-span ratio less than 1/5) was investigated by a wind tunnel test on a scaled model. In addition, the wind pressure coefficient and fluctuating wind pressure under different typical wind directions were obtained. Moreover, ANSYS software and midas gen software were used to simulate the wind pressure filed of this shallow spherical shell roof structure under different wind directions. The wind-induced responses of this thin spherical shell roof structure provided detailed understanding and enriched corresponding database of large-span spatial roof structure.

2. Wind Tunnel Experiments

2.1. Test Setup. The experiments were conducted in a closed-type wind tunnel at Northwest University of Technology, China, which consists of three alterable sections with a total length of 80 m. Dimensions of the testing section employed are $12 \times 2.5 \times 3.5$ m (length × height × width, $L \times H \times W$). The wind-induced vibrations of spherical shell roof structure were predicted based on the wind tunnel experiment data, and the maximum permissible wind velocity was 90 m/s, and the minimum stable wind velocity was 10 m/s. The wind pressure was measured by the PSI9816 device and the network intelligent pressure data acquisition system based on TCP/TP. The outline of the wind tunnel is shown in Figure 1.

2.2. Experimental Model. The tested model was constructed at 1 : 100 scale by using glass materials with a thickness of 3 mm. The spherical shell roof in the experiment had a length of 0.083 m along the arrow height and 1 m in span, which means the rise-to-span is 1 : 12. The model was deployed on a wood plate with a diameter of 1.9 m, while smooth chamfers were designed around the wood plate. A total of 352 wind pressure measurement points were arranged on the half side of model considering the symmetric characteristic. The sampling frequency was 100 Hz. The air tightness of each pressure line was checked before the installation of the model. The distribution of pressure measurement points is shown in Figure 2.

The directions of wind were selected as 0°, ±45°, ±90°, and 180° (defined by the longitudinal axis of wind tunnel), while the geomorphology and wind profile were neglected in the test. The wind speed was 26.8 m/s.

The average wind pressure coefficient $C_{p,i}$ of each pressure tap under different wind directions was derived by

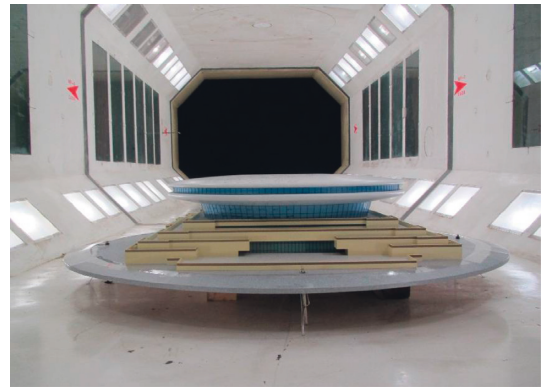

Figure 1: The wind pressure model in wind tunnel.

$$C_{p,i} = \frac{p_i - p_\infty}{(1/2)\rho v^2}, \tag{1}$$

where p_i = pressure at ith point, p_∞ = static pressure of the reference point, and $(1/2)\rho v^2$ = dynamic pressure of the reference point.

The local shape coefficient of model μ_z can be obtained by using wind load ω_k [13], basic wind pressure ω_0, vibration factor β_z, and height variation factor of wind pressure at height z μ_z.

$$\mu_s = \frac{\omega_k}{\omega_0 \cdot \beta_z \cdot \mu_z}, \tag{2}$$

where μ_z can be calculated as

$$\mu_z = 0.478 Z^{0.32}. \tag{3}$$

3. Experimental Results and Discussion

The wind pressure coefficients of six different wind directions are displayed in Figure 3, where m represents the number of pressure measurement points. It can be seen that the pressure of each pressure tap was varied with the change of wind direction, and it is obvious that in some specific areas of the model, the pressure coefficient reached a peak value of −2.5 while the coefficient of other area closed to zero. It is known that the non-full-span distribution of wind pressure possibly leads to more disadvantages on the mechanical performance of structures compared with the case of full-span distribution. Therefore, it is necessary to obtain the actual distribution of wind pressure on the complex structures. Seven replication experiments were conducted to achieve the coefficient of wind pressure under the wind direction of 0°, and the test results are shown in Table 1. It was obtained that the results of different experiments in the present study showed a relatively higher level of repeatability, which indicates that the results of present experimental investigation assumed typical response of thin spherical shell roof structures.

Figure 4 shows the local shape coefficients of the model under wind directions employed in this study according to equations (2) and (3). It is considered that the wind

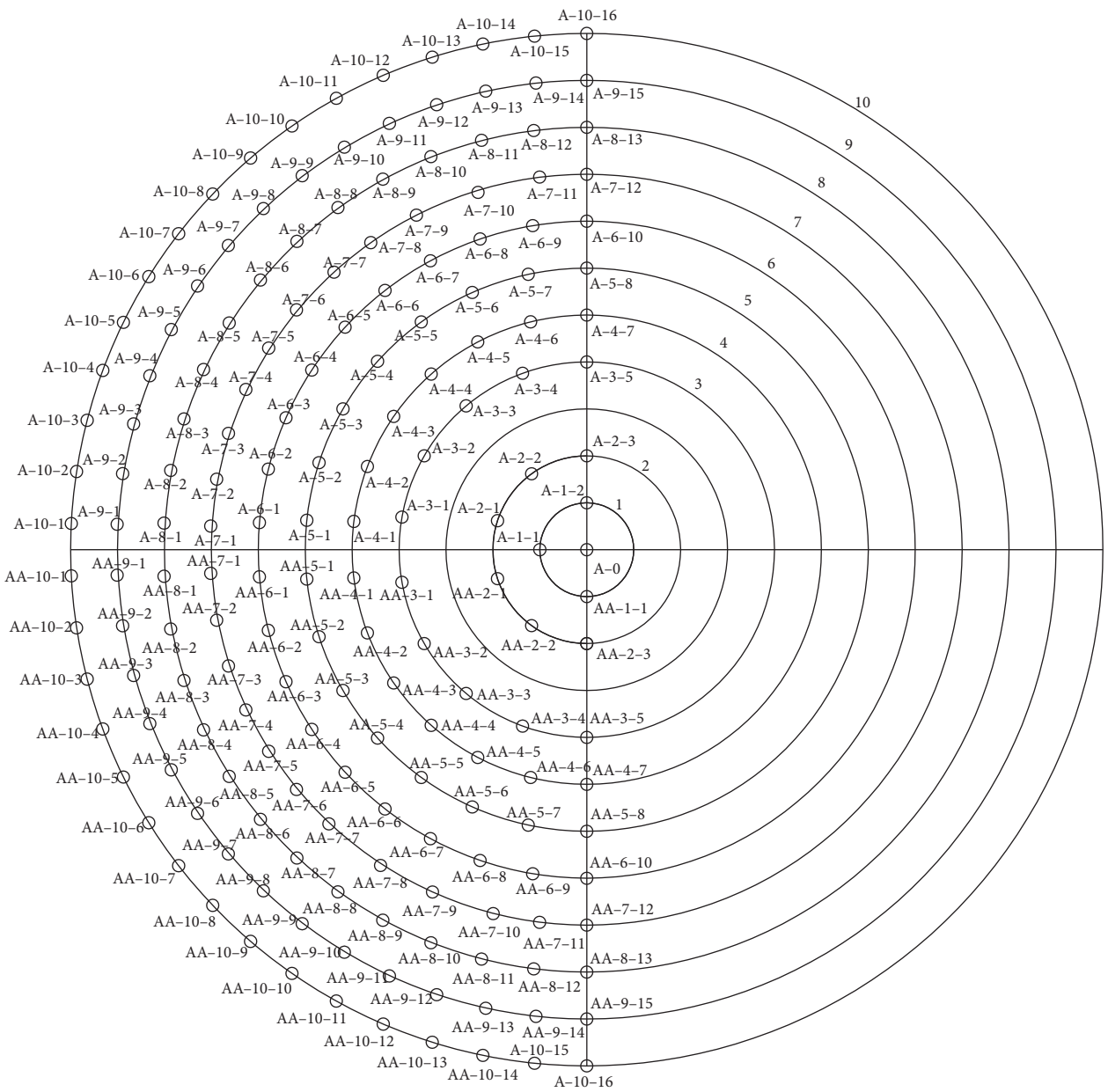

Figure 2: Pressure measurement points on the model.

pressure of the model appeared as suction forces upward owing to the negative value of wind pressure with the wind directions between 0 and 90 degrees, and the shape coefficients of the forward area of the model possessed a declination attributed to the separation zone in front of the roof. Simultaneously, the variation in shape coefficients of the backward of the model showed a smoothly increasing alteration as a result of the existence of reattachment zone at this area.

Figure 5 presents the pressure nephogram and isobaric line of the shallow shell spherical roof with different wind directions in the wind tunnel test. It was observed that the maximum suction forces of wind on the surface of roof occurred at the lateral side of edge on the upwind side, and it was worth noting that the distribution of wind pressure on the thin spherical shell roof differs from that of spherical shell roof; the separation of wind pressure was moderate owing to the relatively small suction force caused by wind.

Furthermore, wind pressures on the surface of shallow spherical shell roof were of negative values, and the wind load on the roof was dominated by suction forces, while the maximum suction force was observed at the top of the roof surface, which was induced by the flow acceleration along the curved surface at this area. In conclusion, the wind tunnel test suggests that the aerodynamic shape of shallow spherical shell roof can be improved to reduce the influence of wind load.

4. Finite Element (FE) Analysis

To compare the results from tests and the performance of unscaled structure, the finite element model of original

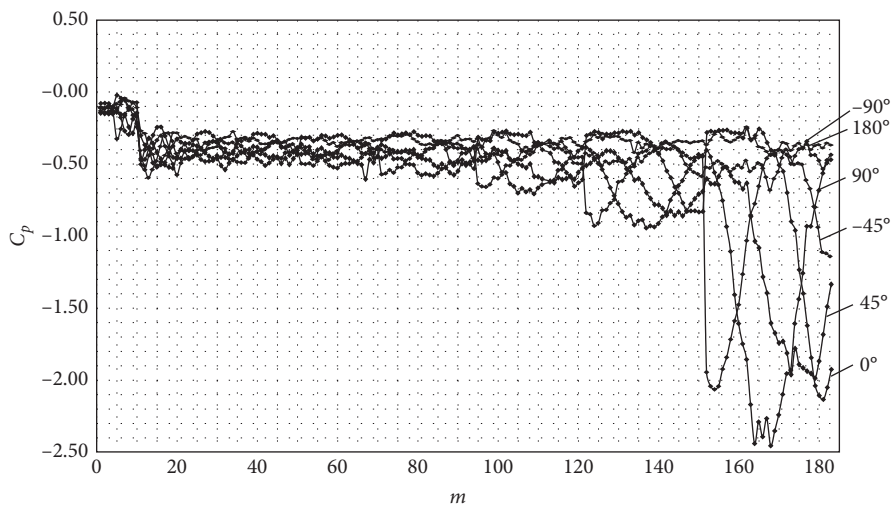

Figure 3: The wind pressure coefficient under six different wind directions.

Table 1: Seven repetitive test results under the wind direction of 0°.

Pressure taps	1	2	3	4	5	6	7
A-0	−0.079	−0.079	−0.078	−0.078	−0.080	−0.078	−0.079
A-9-15	−0.830	−0.831	−0.831	−0.830	−0.833	−0.830	−0.830
B-1-1	0.384	0.379	0.375	0.379	0.379	0.382	0.379
B-1-15	−0.564	−0.564	−0.564	−0.566	−0.566	−0.563	−0.563
C-1-12	0.833	0.832	0.833	0.833	0.832	0.827	0.832
C-3-9	−0.020	−0.023	−0.025	−0.025	−0.025	−0.023	−0.021
D-1-11	−0.581	−0.581	−0.583	−0.588	−0.581	−0.587	−0.583
D-2-12	−0.605	−0.609	−0.613	−0.616	−0.608	−0.612	−0.608

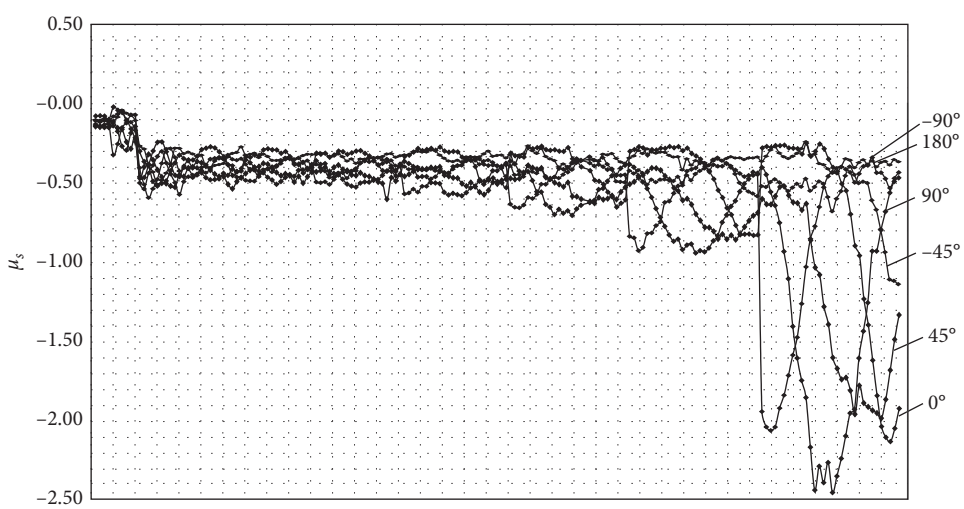

Figure 4: Local shape coefficients of the model. Wind direction of (a) 0°, (b) 45°, (c) 90°, (d) 180°, (e) −90°, and (f) −45°.

structure was developed by using the ANSYS software to obtain specific responses, as shown in Figure 6. The wind load was applied to the model according to the test.

Under Cartesian coordinates, the three-dimensional compressible unsteady Navier–Stokes equations in integral form can be written as

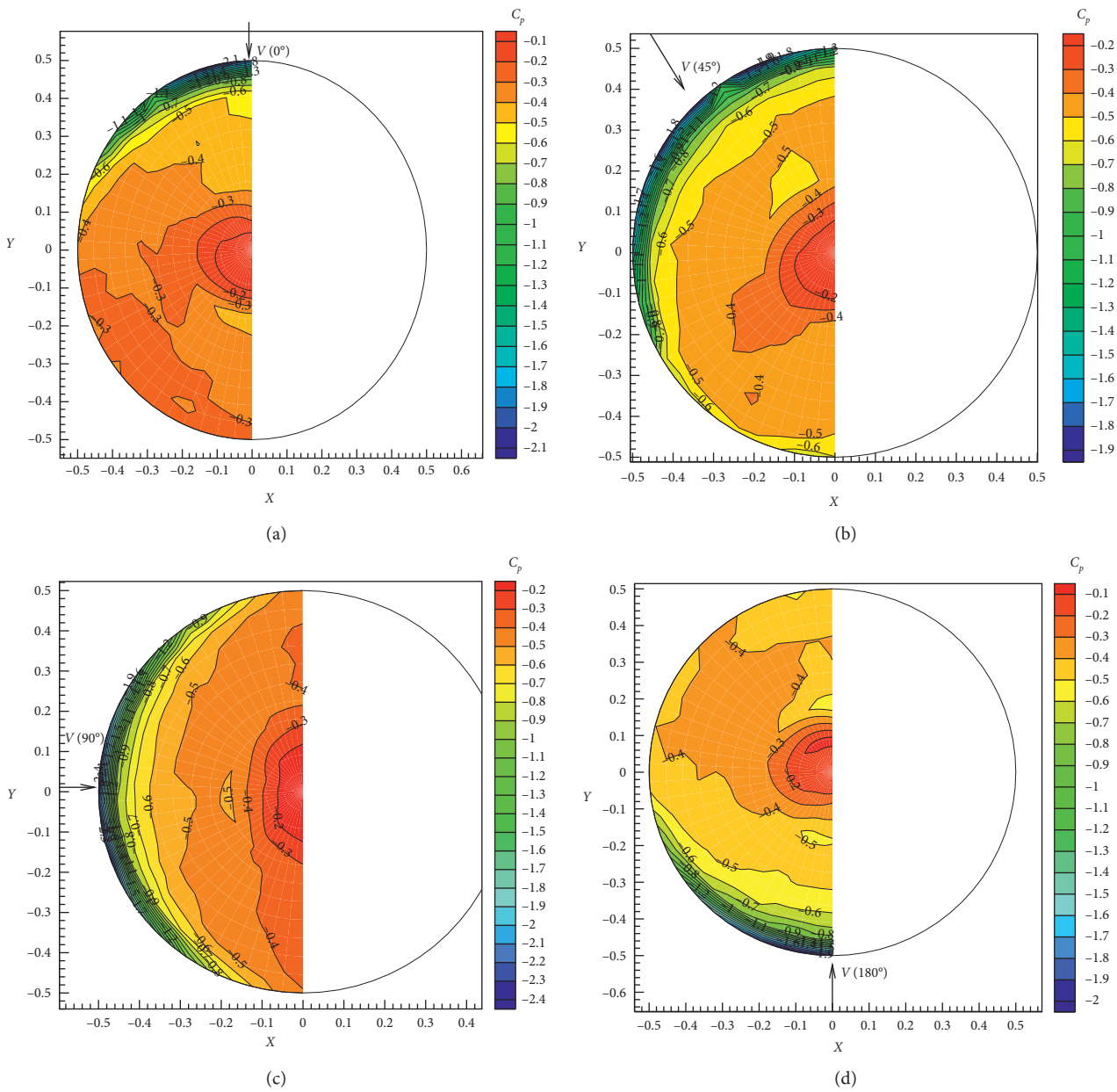

Figure 5: Continued.

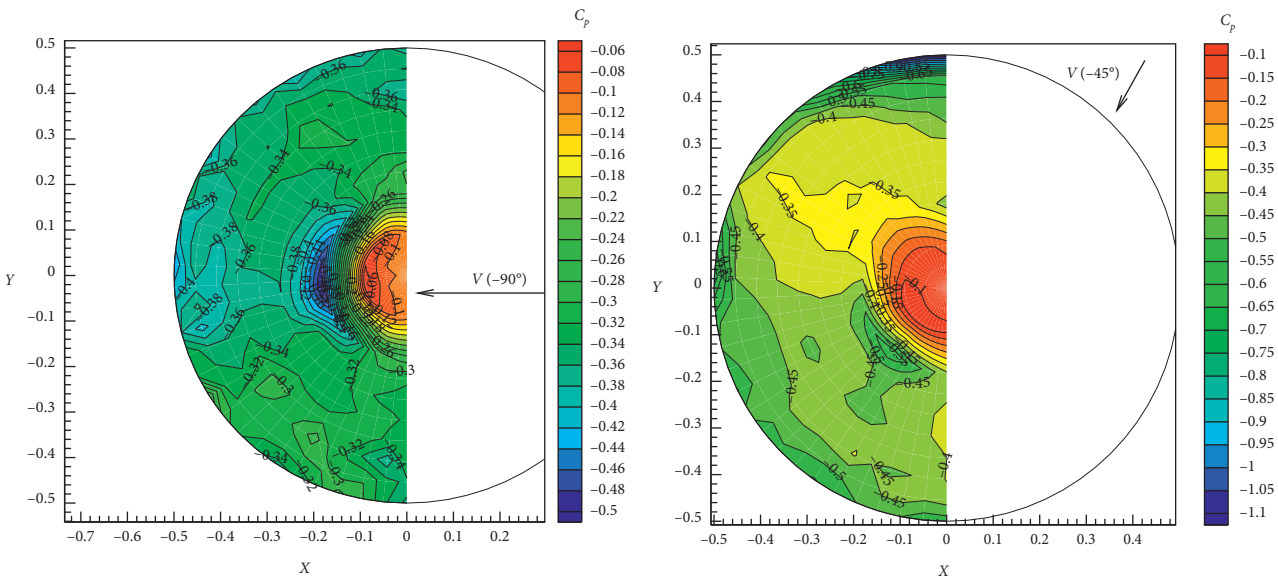

(e) (f)

Figure 5: The pressure nephogram and isobaric line of shallow shell spherical roof.

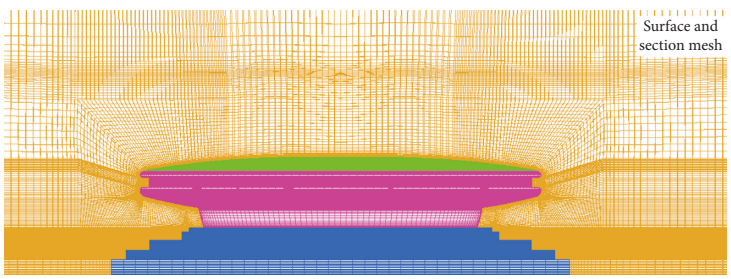

Figure 6: Finite element modelling of structure.

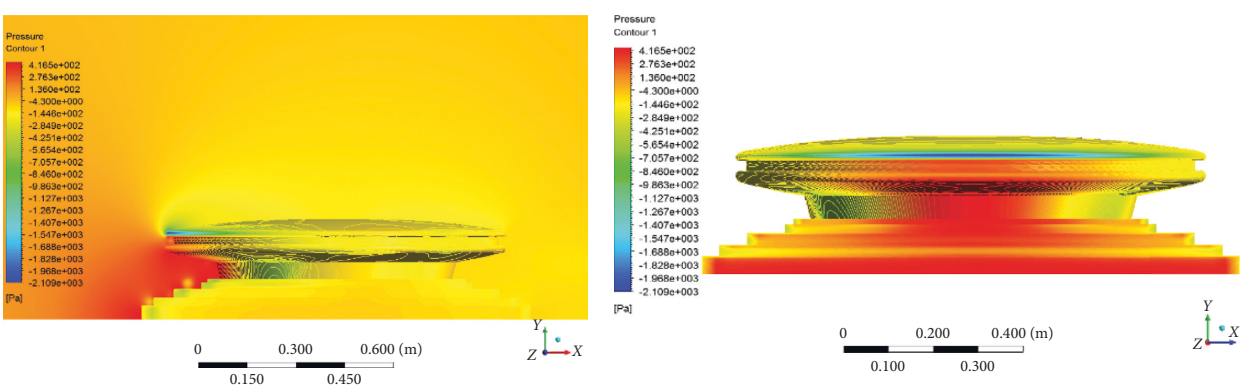

(a) (b)

Figure 7: Continued.

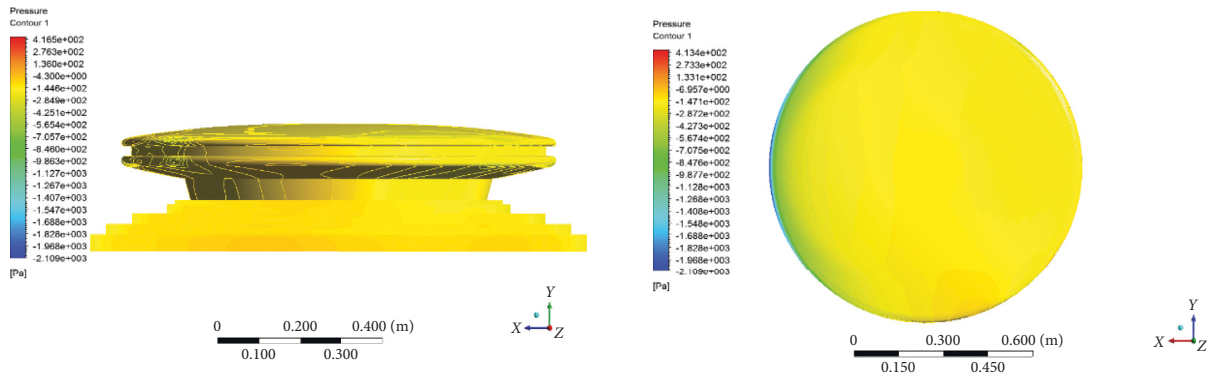

(c) (d)

Figure 7: Results of FE analysis. (a) Lateral side of the model. (b) Windward side. (c) Leeside of the model. (d) Shell roof.

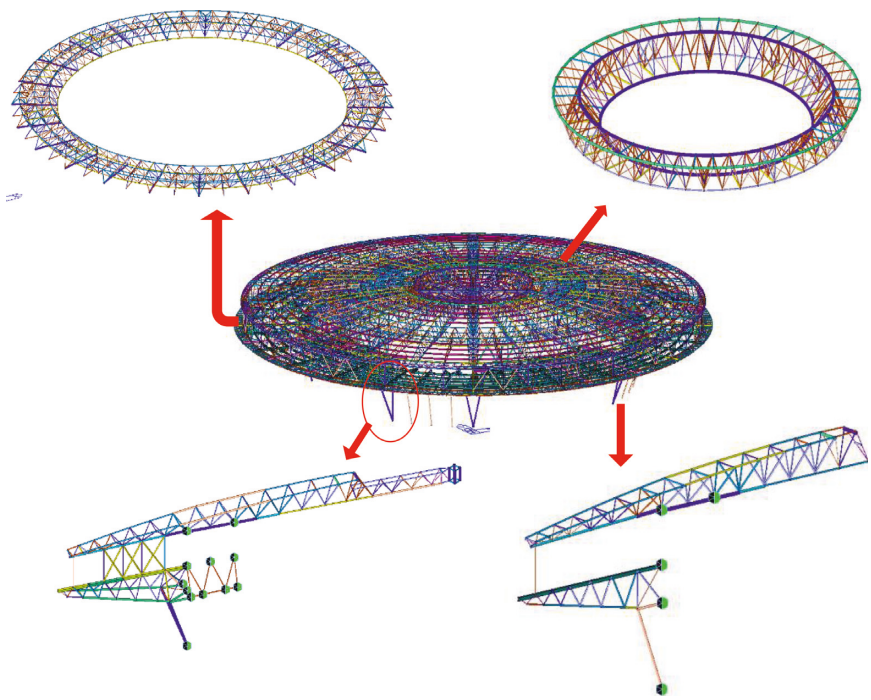

Figure 8: Finite element modelling of structure.

Table 2: Basic load conditions applied to the model.

Conditions	Type of load	Wind load (kN/m^2)
1	Dead load	1.13/1.83
2	Live load	0.5
3	Live load	4.5

Table 3: Results of modal analysis.

Modals	Frequency		Period (s)
	rad/s	Cycle/s	
1	6.9679	1.109	0.9017
2	7.8129	1.2435	0.8042
3	9.566	1.5225	0.6568
4	10.565	1.6815	0.5947
5	14.4582	2.3011	0.4346

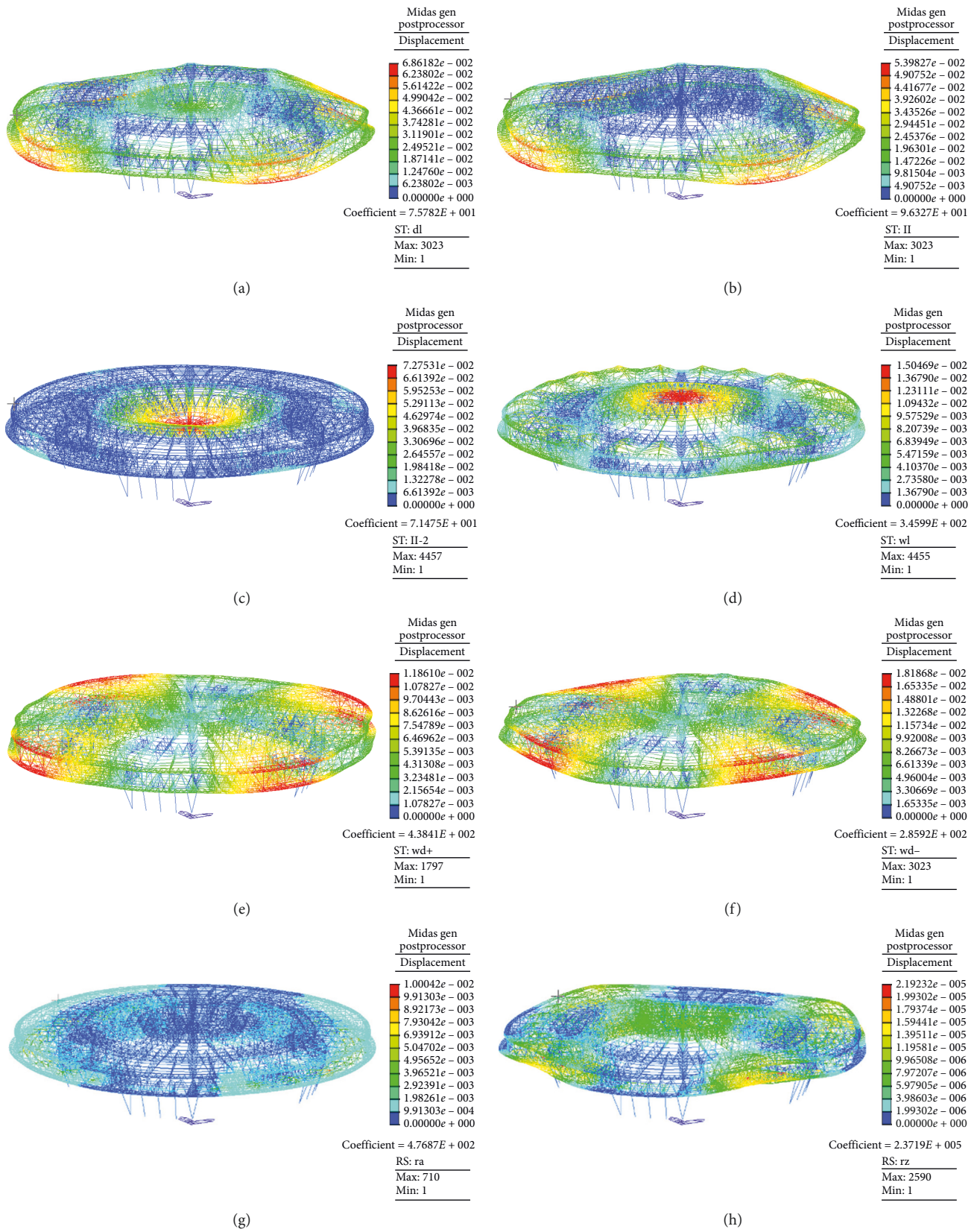

Figure 9: Displacements of nodes in the FE model under different load conditions. (a) Condition 1. (b) Condition 2. (c) Condition 3. (d) Condition of wind load. (e) Condition of increasing temperature. (f) Condition of decreasing temperature. (g) Condition of horizontal seismic. (h) Condition of horizontal seismic.

Table 4: Envelope values of stress in FE model under different load conditions.

Elements	σ_{max} (kN·m^{-2})	σ_{min} (kN·m^{-2})	Elements	σ_{max} (kN·m^{-2})	σ_{min} (kN·m^{-2})	Elements	σ_{max} (kN·m^{-2})	σ_{min} (kN·m^{-2})
90835	59.2	−63.5	91411	56.4	−65.8	91699	−42.0	−57.3
90837	26.0	−56.9	91413	25.2	−59.7	91700	−44.3	−68.3
90839	61.8	−33.4	91415	61.0	−39.0	91701	−25.5	−47.2
90841	81.7	15.1	91417	80.4	−12.0	91702	18.3	−30.7
90843	144.0	51.3	91419	143.0	42.8	91703	54.0	9.2
90845	205.0	24.6	91421	205.0	17.0	91704	103.0	−19.9
90846	146.0	−67.1	91422	146.0	−73.7	92250	−41.7	−80.4
90849	122.0	−91.4	91425	122.0	−96.5	92257	−49.1	−63.2
90852	79.8	−34.0	91428	78.8	−39.3	92258	−41.5	−55.4
90855	70.0	53.1	91431	69.0	47.6	92259	−22.6	−49.5
90858	61.4	59.3	91434	59.4	55.7	92260	21.5	−33.1
90861	61.3	30.3	91437	60.4	26.6	92261	58.5	7.9
90864	21.7	−30.3	91440	20.9	−32.8	92262	107.0	−17.7
90865	−19.1	−67.6	91441	−19.6	−69.4			

Table 5: Envelope values of displacements of nodes in the FE model under different load conditions.

Nodes	δ_x (mm)	δ_y (mm)	δ_z (mm)	Nodes	δ_x (mm)	δ_y (mm)	δ_z (mm)
5403	−0.56	0.20	−11.64	7062	0.26	0.27	−6.32
5406	−0.70	0.22	−10.38	7063	0.43	0.27	−5.03
5409	−0.81	0.23	−9.16	7064	0.65	0.26	−3.98
5412	−0.95	0.21	−7.41	7213	0.32	0.22	−14.4
5413	−0.82	0.23	−5.15	7215	0.49	0.22	−13.4
5415	−1.04	0.09	−5.48	7231	1.10	0.12	−4.34
5474	0.18	0.27	−7.97	7233	0.93	0.16	−3.59
5475	−0.09	0.26	−6.48	7247	−0.09	0.28	−9.06
5476	−0.26	0.26	−5.12	7268	−0.18	0.28	−10.2
5477	−0.49	0.24	−4.00	9525	0.61	1.27	−3.23
5597	−0.21	0.18	−14.08	9546	0.07	0.32	−10.8
5598	−0.37	0.18	−13.05	9572	0.05	0.29	−14.0
5711	0.26	0.27	−9.33	9573	0.03	0.30	−13.5
5712	0.36	0.25	−10.50	9589	0.11	0.28	−14.1
5714	−0.77	0.13	−3.55	9593	0.14	0.28	−13.7
6997	0.69	0.24	−11.94	9636	0.03	0.30	−12.5
6999	0.83	0.26	−10.65	9638	0.06	0.31	−11.5
7003	0.95	0.27	−9.39	9684	0.15	0.28	−12.8
7005	1.09	0.25	−7.59	9685	0.12	0.30	−11.8
7009	1.19	0.13	−5.62	9772	0.07	0.30	−14.1
7061	0.12	0.28	−7.75	9776	0.09	0.28	−14.1

$$\frac{\partial}{\partial t}\iiint_{\Omega}\mathbf{Q}\,\mathrm{d}V + \oiint_{\partial\Omega}\mathbf{F}\cdot\vec{\mathbf{n}}\,\mathrm{d}S = 0, \tag{4}$$

where $\mathbf{Q} = (\rho, \rho u, \rho v, \rho w, \rho e)^T$ denotes the solution vector, $\partial\Omega$ denotes the boundary of integral domain, $\vec{\mathbf{n}}$ denotes the normal vector directing outward of integral domain, and t is time.

To well capture the unsteady boundary layer separation induced by shockwave in transonic flow, the shear stress transport (SST) k-ω turbulence model is chosen to enclose Navier–Stokes equations for steady state simulations. The transport equations for turbulence energy k and dissipation rate ω can be written as follows:

$$\begin{aligned}\frac{\partial(\boldsymbol{\rho}\mathbf{k})}{\partial\mathbf{t}} + \frac{\partial(\boldsymbol{\rho}\mathbf{k}\mathbf{u}_\mathbf{i})}{\partial\mathbf{x}_\mathbf{i}} &= \frac{\partial}{\partial\mathbf{x}_\mathbf{j}}\left(\Gamma_\mathbf{k}\frac{\partial\mathbf{k}}{\partial\mathbf{x}_\mathbf{j}}\right) + \widetilde{\mathbf{G}}_\mathbf{k} - \mathbf{Y}_\mathbf{k},\\ \frac{\partial(\boldsymbol{\rho}\boldsymbol{\omega})}{\partial\mathbf{t}} + \frac{\partial(\boldsymbol{\rho}\boldsymbol{\omega}\mathbf{u}_\mathbf{i})}{\partial\mathbf{x}_\mathbf{i}} &= \frac{\partial}{\partial\mathbf{x}_\mathbf{j}}\left(\Gamma_\boldsymbol{\omega}\frac{\partial\boldsymbol{\omega}}{\partial\mathbf{x}_\mathbf{j}}\right) + \mathbf{G}_\boldsymbol{\omega} - \mathbf{Y}_\boldsymbol{\omega} + \mathbf{D}_\boldsymbol{\omega}.\end{aligned} \tag{5}$$

For both inviscid and viscous terms in Navier–Stokes equations, the second-order upwind scheme proposed by Barth and Jesperson is employed.

Figure 7 presents the results of FE analysis. The wind pressure yields greater values between the shell roof and the ground, while the wind appeared to separate at the steps, leading to the vortex in the form of low pressure. Due to blunt body of the model, the pressure in the middle position is the highest, with the flow of air from the middle to both sides and above; the pressure gradually decreases, and the change of pressure is directly related to the local windward area, and under the condition of flow separation, the pressure recovery on the leeward side is low, and the total pressure on the leeward side is lower than that on the upwind side. On the windward side of the top cover, the effect of flow around is more obvious; while moving from the symmetrical position to both sides, the effect of flow acceleration gradually weakens. By making comparisons between Figures 7 and 5, it can be concluded that distributions

of wind pressure obtained by FE method and tests are similar, which somewhat confirms the validity of FE analysis.

The midas gen software was used to simulate the response of unscaled structure. The truss element was employed to establish the finite element model, as shown in Figure 8. The dead loads and live loads are selected according to the practical engineering, yet the deadweight of structure was not included.

The wind load ω_k was calculated by equation (2), where μ_z was taken as 1.7 in accordance with the test results, and μ_s, μ_z, and ω_0 were determined according to GB 50009-2012 [13].

Three load conditions, including dead loads, live loads, seismic loads, and wind loads, were applied to the model to conduct the finite element analysis. The specific information of basic load conditions is listed in Table 2. Specially, for the purpose of considering the seismic action, the modal analysis was carried out in order to transfer seismic loads into static forces, and the results are organized in Table 3. Moreover, the influence of temperature change on the structure was taken into consideration, and ranges of 15–30 and 8–15 degrees were selected as cases for temperature change.

The node displacements of finite element (FE) model under three load conditions, seismic loads, and temperature loads are shown in Figure 9. It was concluded that the performance of structure under each single load condition is favorable on the basis of the limited displacement of nodes in the FE model. So, combinations of these load conditions were made to investigate the performance of the structure under various load conditions. The combinations of loads are referred to the form as

$$\lambda_t = \eta_1\lambda_1 + \eta_2\lambda_2 + \eta_3\lambda_3 + \eta_4\lambda_4 + \eta_5\lambda_5 + \eta_6\lambda_6, \qquad (6)$$

where λ_t = combined load condition; λ_1, λ_2, and λ_3 = three basic load conditions; λ_4 and λ_5 = vertical and horizontal seismic loads, respectively; λ_6 = load condition of temperature; η_1, η_2, and η_3 = coefficients of three basic load conditions, respectively, which reflect the contribution of each load condition to the final combination of load conditions; η_4 and η_5 = coefficients of the vertical and horizontal seismic loads; and η_6 = coefficient of the temperature loads.

Twenty-one conditions were analyzed by the FE method, and the allowable stresses method was used to evaluate the performance of structure under different load conditions. Tables 4 and 5 present the envelope values of stress and strip displacements at the midspan of shell under all cases obtained by FE analysis, where $\sigma_{\max}$, $\sigma_{\min}$, δ_x, δ_y, and δ_z represents the maximum stress and minimum stress of elements, and displacements of node at directions x, y, and z regarding all load conditions, respectively. It can be seen that the maximum and minimum values in Tables 4 and 5 varied in a finite range, which suggests that the structure gives a nonuniform distribution of wind load, yet the limited value rarely influenced the performance of structure.

Figure 10 shows the maximum predicted-to-permitted stress ratio (α), which includes the results of all load conditions (q). Regardless of the symmetric structure, the complexity of load conditions applied to the FE model lead to great variation in the ratios. Yet the ratios in Figure 8 illustrates that the maximum stress of members in the structure did not exceed the permission, which means the stiffness and strength of structure perform well under the wind load, and furthermore, the safety of structure was confirmed.

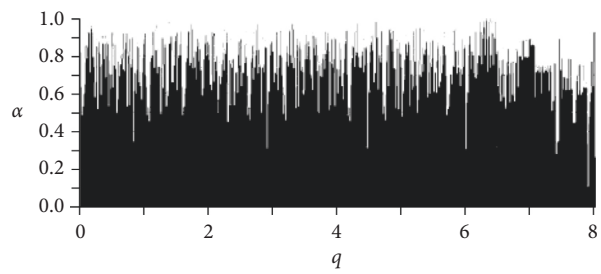

Figure 10: Stress ratio in all load conditions.

5. Conclusions

In this study, wind tunnel tests as well as the numerical simulation of large-span spherical shell roof structure when subjected to different typical wind directions were implemented to investigate its wind pressure characteristics. Wind force coefficients and shape coefficients were obtained to analyze the distribution of wind pressure on the roof structure, and the following conclusions can be summarized:

(1) Both wind force coefficients and shape coefficients change significantly with wind directions, and peak coefficients were obtained at 90°.

(2) For this spherical shell roof, most parts during test were subjected to negative wind pressure, i.e., suction force. Flow separation phenomenon occurred in the windward areas, and accordingly, the maximum negative value was observed at the top of the roof surface. The experimental results proved that the geometry of this spherical shell roof had good mechanical performance.

(3) The dynamic performance of spherical shell roof structure under wind load was studied with numerical method. Twenty-one load cases including the dead loads, live loads, seismic loads, and temperature loads were combined and applied to the FE model. The structure showed a desirable performance under employed load cases, and the stress and displacement of members varied within a permitted range.

Data Availability

No data were used to support this study.

Conflicts of Interest

The authors declared that there are no conflicts of interest.

Acknowledgments

The authors gratefully acknowledge the financial supports for this research by the Natural Science Foundation of China, China (grant no. 51508028), and the Fundamental Research Funds for the Central Universities (grant no. 310828173402).

References

[1] D. P. Billington, *Thin Shell Concrete Structures*, McGraw-Hill, New York, NY, USA, 2nd edition, 1982.

[2] H. C. Noh, "Ultimate strength of large scale reinforced concrete thin shell structures," *Thin-Walled Structures*, vol. 43, no. 9, pp. 1418–1443, 2005.

[3] Z.-T. Chang, M. A. Bradford, and R. I. Gilbert, "Short-term behaviour of shallow thin-walled concrete dome under uniform external pressure," *Thin-Walled Structures*, vol. 49, no. 1, pp. 112–120, 2011.

[4] R. P. Hoxey and A. P. Robertson, "Pressure coefficients for low-rise building envelopes derived from full-scale experiments," *Journal of Wind Engineering and Industrial Aerodynamics*, vol. 53, no. 1-2, pp. 283–297, 1994.

[5] Y. Uematsu, M. Yamada, A. Inoue, and T. Hongo, "Wind loads and wind-induced dynamic behavior of a single-layer latticed dome," *Journal of Wind Engineering and Industrial Aerodynamics*, vol. 66, no. 3, pp. 227–248, 1997.

[6] J. Fu, Q. Zheng, J. Wu, and A. Xu, "Full-scale tests of wind effects on a long span roof structure," *Earthquake Engineering and Engineering Vibration*, vol. 14, no. 2, pp. 361–372, 2015.

[7] Y. Uematsu, T. Moteki, and T. Hongo, "Model of wind pressure field on circular flat roofs and its application to load estimation," *Journal of Wind Engineering and Industrial Aerodynamics*, vol. 96, no. 6-7, pp. 1003–1014, 2008.

[8] Y. Uematsu, K. Watanabe, A. Sasaki, M. Yamada, and T. Hongo, "Wind-induced dynamic response and resultant load estimation of a circular flat roof," *Journal of Wind Engineering and Industrial Aerodynamics*, vol. 83, no. 1–3, pp. 251–261, 1999.

[9] P. Biagini, C. Borri, and L. Facchini, "Wind response of large roofs of stadions and arena," *Journal of Wind Engineering and Industrial Aerodynamics*, vol. 95, no. 9-11, pp. 871–887, 2007.

[10] H. Marukawa, Y. Uematsu, Y. Tamura et al., "Design wind load on a flat long-pan roof," in *Proceedings of the 4th East Asia-acific Conference on Structural Engineering and Construction*, Y. K. Shin, S. P. Chang, and H. M. Koh, Eds., vol. 3, pp. 1619–1624, Seoul, Korea, September 1993.

[11] T. Hongo, *Experimental Study of Wind Forces on Spherical Roofs*, Ph.D. thesis, Tohoku University, Sendai, Japan, 1995.

[12] X. Zhou, Z. Han, M. Gu, A.-A. Zhang, W. Zhang, and W. Fang, "Research on wind-induced responses of a large-scale membrane structure," *Earthquake Engineering and Engineering Vibration*, vol. 12, no. 2, pp. 297–305, 2013.

[13] CS (Chinese Standard) GB 50009-2012, *Load Code for the Design of Building structures*, Ministry of Construction of the People's Republic of China and Quality Supervision Inspection and Quarantine of the People's Republic of China, Beijing, China, 2012, in Chinese.